Article

One Pot Synthesis, Surface, and Magnetic Properties of Ni–NiO@C Nanocomposites

Ghadah M. Al-Senani [1], Foziah F. Al-Fawzan [1], Mashael Alshabanat [1], Omar H. Abd-Elkader [2,*], Mai Nasrallah [3] and Mohamed Nasrallah [4]

1 Department of Chemistry, College of Science, Princess Nourah Bint Abdulrahman University, P.O. Box 84428, Riyadh 11671, Saudi Arabia
2 Physics and Astronomy Department, Science College, King Saud University, P.O. Box 2455, Riyadh 11451, Saudi Arabia
3 Faculty of Medicine, Ain Shams University, El-Khalyfa El-Mamoun Street, Abbassia, Cairo 11774, Egypt
4 Faculty of Medicine, Ibn Sina University, Aljerif west block 88, Khartoum 11115, Sudan
* Correspondence: omabdelkader7@ksu.edu.sa

Abstract: An entirely novel and creative technique was employed for producing magnetic Ni–NiO@C nanocomposites, and it was based on the utilization different amounts of finely ground and fully dried olive leaf powders. The resulting nanocomposites were identified and characterized by XRD, FTIR, SEM, EDS, TEM, and Raman techniques. The magnetic and surface characteristics of the composites, as it developed, were further evaluated using the Vibrating-Sample Magnetometer (VSM) and Brunauer–Emmett–Teller (BET) techniques. The results confirmed the success of preparing a Ni–NiO@C nanocomposites, each containing Ni and NiO in crystalline form. Through the morphology of the resulting composites, determined on the basis of an SEM analysis, it became clear to us that the particles were of a semi-spherical shape, with a clear grouping and a definition of their grain boundaries. Comparably, a TEM investigation demonstrated that the composites had a core–shell structure. The surface area of the investigated composites increases as the content of dried olive leaf powders increases due to a significant increase in the total pore volume. These composites illustrated low magnetism (4.874 and 8.648 emu/g) and coercivity (55.203 and 39.639 Oe) for a number of reasons, which will be explained.

Keywords: Ni/NiO; nanocomposites; core–shell structures; Brunauer–Emmett–Teller surface; vibrating-sample magnetometer

1. Introduction

When they are present in composites, the development of novel and distinctive qualities raises the significance of elements or their oxides. Composite-based systems possess multiple components and different properties and characteristics, in contrast with single-component systems. The simultaneous existence of many components within the composite frequently causes interactions between them. This coexistence additionally influences the particle size and shape, leading to an influence on the chemical and physical characteristics of the components. Therefore, multi-component systems have more comprehensive applications than single-component systems [1–4]. Multi-component-based magnetic systems exhibit novel and unique properties depending on the size, structure, and composition of the components.

Whenever an element and its oxide—such as nickel and nickel oxide—are incorporated, the composite's structural, electrical, morphological, surface, and magnetic properties are significantly altered. This is because the possibility of each the elements undergoing an electronic transition arises, which increases flaws and exerts an impact on grain boundaries.

Nickel-based materials have gained significant attention recently because of their use in a number of significant disciplines, such as hydrogen fuel cell electrodes, catalytic

reactions, gas detection, super capacitors, smart windows, data storage, and spintronic devices [5,6]. In addition, a wide range of applications of composites containing Ni and NiO are due to thermal stability, magnetic behavior, and a combination between the ferromagnetic (FM) of Ni and the antiferromagnetic (AFM) of NiO as an AFM–FM exchange coupling [1,7]. These technologies have been employed in a variety of disciplines, including batteries powered by lithium ions, electro-catalysts for the process of hydrogen evolution, and the electrochemical storage of energy [7,8]. Moreover, the unique properties of the Ni/NiO nanocomposite rely on the correlation between composition, morphology, crystalline phases, and the dimension of grains [9,10].

During the manufacturing process, the composition of Ni–NiO hetero-structures, the formation of crystals, and the perfection of the hetero-structures are modified as well as controlled [1]. Numerous methods are used to create Ni–NiO composites, such as chemical-based precipitation, sol–gel, hydrothermal process growth, solvothermal synthesis, microemulsion, solid-state chemical degradation, ball milling, the organometallic approach, and magnetron plasma [11–14]. Some authors have indicated the preparation of Ni–NiO composites by first preparing a nickel metal through the urea-assisted auto-combustion method, then oxidizing some of the metallic nickel through calcination at temperatures of 600 and 1000 °C for 2 h to ultimately obtain the intended composites [15]. However, Ni–NiO composites have been obtained by the thermally induced oxidation of metallic green compacts at temperatures between 300 and 450 °C and further sintering [16]. Anisotropic heterogeneous Ni–NiO nanoparticles with controlled compositions are grown using a high-power pulsed hollow cathode process [17]. These approaches are not available without a protracted amount of time required for their interaction with individuals as well as the completion of numerous tasks that drain resources, harm the environment, and consume significant amounts of time and energy. Hence, the pursuit of a vital, environmentally friendly path that leads to a reduction in environmental pollution and the consumption of time, effort, and energy is paramount. The combustion process, which had several benefits, including speed, cost effectiveness, and low temperature requirements, was successful in achieving this goal [18]. In this regard, Deraz referred to the preparation of a Ni–NiO system using a glycine-assisted combustion method [19]. Ni–NiO nanocomposite was obtained using the dried leaves of Corchorus olitorius assisted combustion method, Deraz created this method, which he dubbed the "incandescent combustion method" for preparing different solid's nanoparticles [1]. In this method, the co-presence of Ni and NiO is partially protected by some graphitic layers. Moreover, extracts from diverse plant components, including the leaves, stems, roots, shoots, flowers, bark, and seeds, serve as fuels in the combustion process to create a variety of environmentally friendly nanoparticles, including silver, gold, and magnetite [20]. The majority of the authors in this field indicated that these fuels serve as reducing and regulating agents for bio-reduction reactions in the creation of various nanoparticles using the combustion method [1,21]. Contrarily, carbon nanocomposite products containing metal nanoparticles such as copper and cobalt, as well as nickel or its oxides, are an excellent substitute for use in a wide range of applications involving magnetic resonance tomography and biomedicine, electrode materials over super capacitors, heterogeneous catalysts for petrochemical processes, and dispersed radiation-absorbing media [22]. A core/shell structure of Ni–NiO, encapsulated in carbon nanospheres (CNS) and coated with few- and multi-layered graphene (FLG and MLG) was prepared using the chemical vapor deposition (CVD) method [23]. Carbon atoms were first placed on the Ni particle surface, which initiated the process. Additionally, CNS was grown for 30 min at 950 °C, while FLG and MLG were synthesized on CNS surfaces for 30 and 50 min, respectively, at 1050 °C. These composites were used as reinforcing nanofillers in the polymer matrix to improve the mechanical and thermal properties of the polypropylene matrix. The importance of the Ni–NiO composite is clear to us from the process above, which demonstrates how the Ni–NiO composite increases in the presence of carbon to obtain a Ni–NiO/C composite. To obtain this composite, it was necessary to search for an easy, simple, and inexpensive method, such as the one we discuss in this manuscript.

In this investigation, dehydrated leaves of olive were used to create a Ni–NiO/C nanocomposite. XRD, FTIR, SEM-EDS, TEM, and Raman approaches were further used to characterize and identify the examined composite. The composite's surface and magnetic properties were developed during the final phases.

2. Materials and Methods

2.1. The Extraction of Chemicals and Plant Material

The Sigma-Aldrich Company provided the chemical substance, which was nickel (II) nitrate hexahydrate with the linear formula Ni $(NO_3)_2 6H_2O$. This analytical grade reagent was used immediately, without any additional purification. Freshly harvested olive leaves were obtained from an adjoining farm.

2.2. Preparation Method

2.2.1. Preparation of Leaf Powder

Fresh olive leaves were first gathered and cleaned with tap water before being rinsed once more with distilled water to remove any remaining contaminants. The young leaves were then chopped into little pieces and allowed to air dry for a full week. Finely crushed leaves that were dried were employed for the production of leaf powder.

2.2.2. Preparation of the Ni–NiO/C Composites

Two samples in the amounts of 0.25 and 0.5 g of the dried olive leaves were combined with 2.91 g of a nickel nitrate precursor solution to generate the S1 and S2 samples. The mixture was concentrated in a Pyrex beaker (100 mL) on a hot plate at 350 degrees Celsius for twenty-five minutes. As it became warmer, the crystal water begun vaporization. Once a beaker reached 350 °C, a considerable amount of foam formed; an explosion flashed in one of the edges, spread through the mass with incandescent combustion, and generated a voluminous and fluffy product in the container.

2.3. Techniques

X-ray powder diffraction and scattering applications were performed employing a platform from the special D8 diffractometer series to evaluate the structural properties of various nanoparticles. The patterns were operated with Cu Kα rays at a voltage of 40 kV, a current of 40 mA, and a scanning speed of 2°/min. The average crystallite dimensions (d), density of dislocations (δ), and stresses (ε) for the freshly prepared composition, which includes nickel and nickel oxide, were calculated using Formulas (1)–(3), relying on the Scherrer formula [21,24]:

$$d = \frac{B\lambda}{\beta \cos\theta} \tag{1}$$

$$\delta = \frac{1}{d^2} \tag{2}$$

$$\varepsilon = \frac{\beta \cos\theta}{4} \tag{3}$$

where B refers to the Scherrer factor (0.89), λ represents the wavelength of the employed X-ray beams, θ indicates the Bragg angle, and β indicates the full width at half maximum (FWHM) of the diffraction peak.

The Fourier-transmission (FTIR) infrared spectra of the investigated material were collected employing a Perkin-Elmer 1430 Relative Recorded Infrared Spectrophotometer (AS IS). A total of 200 mg of vacuum-dried IR-grade potassium bromide (KBr) was mixed with each solid sample, which was individually divided into two milligrams. To measure the FTIR spectra, a range of 4000–400 cm^{-1} was applied. After the mixture had been treated in a vibrating ball mill for three minutes, it was dispersed using a steel die with a 13 mm

diameter. The FTIR spectrophotometer's double-grating spectrophotometer holder was filled with identical discs.

The Raman spectroscopy results of the Ni–NiO/C samples were captured utilizing the 20–100× lenses and i-RAMAN Plus, which is a high quantum efficiency CCD array detector with deeper cooling, a high dynamic range, and a higher signal–noise ratio for up to 30 min of integration time (B&W TEK, Newark, DE, USA).

In order to prepare the samples for quick ultrasonic processing, drops of the reaction mixture were placed over carbon-coated copper grids, and the solvent was allowed to evaporate. The samples were first immersed in ethanol. A JEOL model 1230 instruments (Tokyo, Japan) running at an accelerating voltage of 120 kV was used to conduct TEM measurement.

The JEOL JAX-840A SEM (Tokyo, Japan) captured electron microscopy images of the solids as they were constructed. After being handled, the solid was rinsed in ethanol and ultrasonically adjusted to scatter the individual particles across a thin piece of double-sided carbon tape placed above mount holders.

A non-destructive analytical technique known as energy dispersive X-ray analysis (EDS) is frequently utilized to obtain elemental information from solid materials. EDS was carried out on a JEOL (JED-2200 Series) electron microscopy unit coupled with a Kevex Delta system. The window width was set to 8 m, the accumulation time was 100 s, and the accelerating voltage was set to 15 kV. Surface molar composition was established using the Asa method, Zaf rectification, and Gauss estimation.

Using the Nova 2000 Quanta Chrome (commercial BET unit) at 350 °C, the particular area of the surface (S_{BET}), overall volume of pores (V_p), and average pore size (ŕ) of a number of solids were calculated. Each sample was degassed for two hours at 200 °C prior to conducting these experiments, under a decreased pressure of 10^{-5} Torr.

With a maximum applied field of 20 KOe, a magnetometer with a vibrating sample (VSM; 9600-1 LDJ, Troy, MI, USA) was employed to evaluate the studied solid's magnetism at room temperature. The saturation (M_s) and remanence (M_r) magnetizations, the squarence (M_r/M_s), the coercivity (H_c), and the anisotropy (K_a) were all calculated from the hysteresis loops that were acquired.

3. Results

3.1. Structural Analysis

X-ray analysis was employed to determine the purity and degree of crystallinity in an effort to establish the physical properties of the investigated composites. Figure 1 demonstrates the XRD patterns for the composite studied. This figure indicated that these composites contain some crystalline phases that were identified using the Joint Committee on Powder Diffraction File Standards (PDF). The examined composites' XRD patterns demonstrate that both nickel and nickel oxide phases are present in composites. The stated values in PDF files Numbers 04-0850 and 04.0835 correspond closely with the cubic structure and space group Fm3m associated with these phases, respectively. This is supported by the observation that the main nickel oxide peaks occurred at 2θ = 37.23°, 43.26°, 62.86°, 75.93°, and 79.36° for the S2 sample; while they occurred at 2θ = 37.14°, 43.18°, 62.78°, 75.21°, and 79.27° for the S1 sample with planes (111), (200), (220), (311), and (222), respectively. However, the most significant Ni-related peaks were identified at 2θ = 44.76°, 51.75° and 79.10° for the S2 sample; while they were identified at 2θ = 44.35°, 51.74°, and 79° for the S1 sample with planes (111), (200), and (220), respectively. This denotes an alteration in the exact location of many peaks associated with the nickel and nickel oxide phases. Furthermore, it was noted that a steep decline in the height peaks of NiO was countered by an increase in those of Ni, providing further evidence of the phase transition event. Regardless of the manner in which we use the dry the olive leaves and the existence of traces of carbon, a combustion by-product that is not visible in the XRD pattern due to its small quantity cannot be discarded.
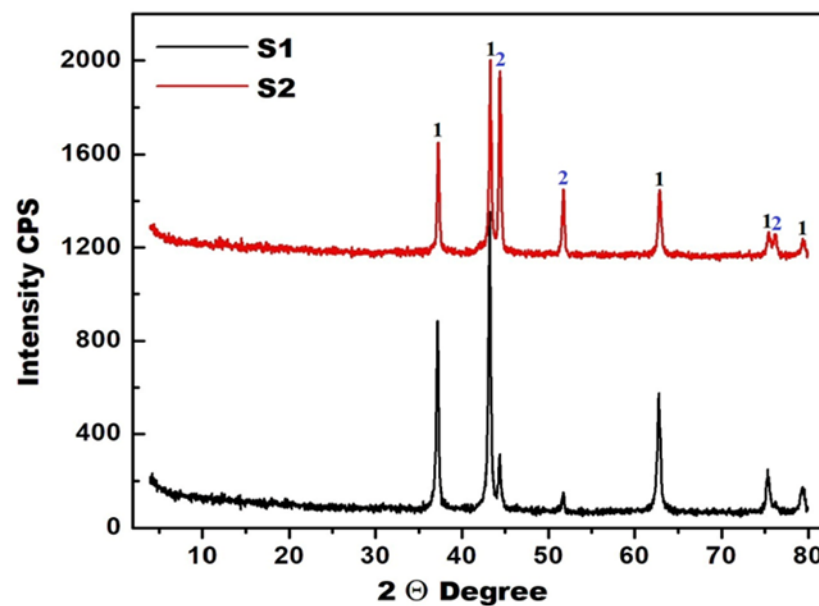
Figure 1. X-ray Diffraction of Ni–NiO@C composites where 1 is Ni and 2 is NiO.

Our ability to compute certain structural characteristics of the investigated composites, such as the crystallite size (d), lattice constant (a), X-ray density (D_x), and unit cell volume (V) of crystalline phases, is made possible by the results of X-ray experiments. Table 1 lists the computed values for several structural parameters of the S1 and S2 samples. This table shows that the "d, a, and V" values of NiO are greater than those of Ni. The dislocation δ, strain ε, and X-ray density D_x values all displayed opposite behavior. When the amount of olive leaves was increased, the values of d and D_x for both Ni and NiO increased slightly, whereas the values of a, V, and d decreased.

**Table 1.** The crystalline Nickel and Nickel oxide phase's structural features within the S1 as well as S2 samples.

Parameters	Nickel Oxide		Nickel	
	S1	**S2**	**S1**	**S2**
d, nm	37	41	32	35
a, nm	0.4187	0.4180	0.3535	0.3534
V, nm^3	7.340	7.301	4.417	4.412
D_x, g/cc	6.757	6.794	8.823	8.834
δ, Lines/nm^2	7.30×10^{-4}	5.95×10^{-4}	9.76×10^{-4}	8.16×10^{-4}
ε	0.0026	0.00242	0.0030	0.0028

3.2. FTIR Analysis

FTIR spectra were conducted on the S1 and S2 samples to investigate the various characteristic functional groups associated with these composites. Figure 2 demonstrates the FTIR spectra of the prepared samples. This figure displays absorption bands between 4000 and 400 cm^{-1}. It is obvious that there are some absorption bands located between 1000 and 400 cm^{-1}, which belong to the metal-oxygen vibration mode [3]. A typical sharp band appears at 418 cm^{-1}. It is related to metal oxide stretching vibrations of the Ni–O bond. Broad bands at 556, 660, and 1023–991 cm^{-1} correspond to the Ni-OH group [5]. The bands located at 1107–1103, 1195, and 1368–1347 cm^{-1} indicate the existence of carbonates, while the band at 2937 cm^{-1} corresponds to the C-H stretching mode [3]. The broad bands at 1665–1636 and 3383–3051 cm^{-1} belong to the stretching vibrations of O-H bonds, indicating the presence of moisture generated during the preparation of the IR pellet [3]. We notice that the intensity of the observed bands in the S2 sample is less than that in the S1 sample,

with a severe decrease in the intensity of the band at 556 cm^{-1}. However, there is a shift in the positions of the bands. These findings may be due to a phase transition of some NiO to Ni, and this is consistent with both XRD results and what is confirmed later.
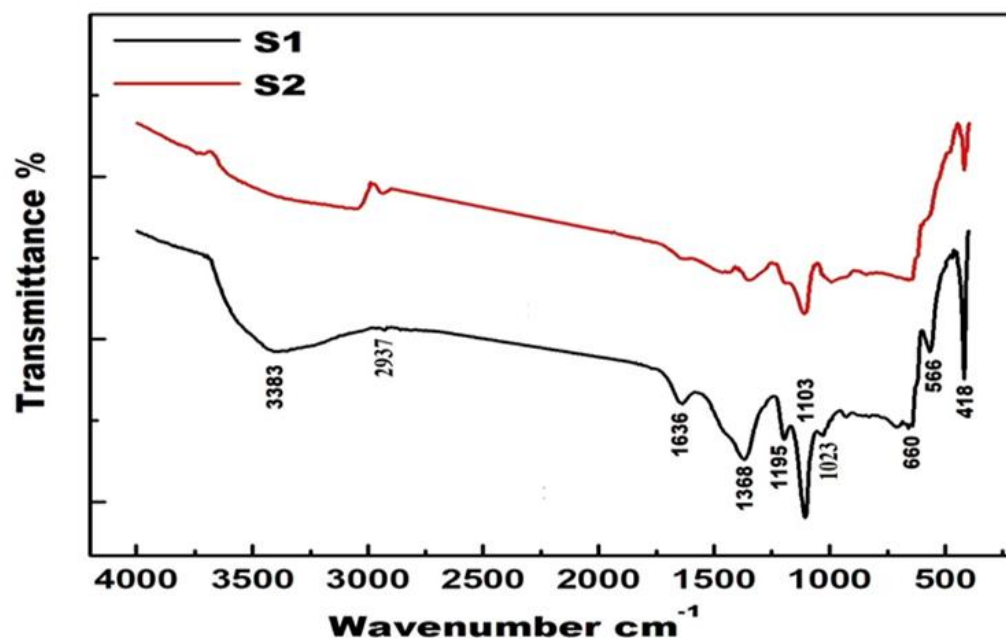
Figure 2. FTIR Spectra of the S1 and S2 samples.

3.3. Raman Analysis

The polarization-induced vibrations of the S1 and S2 samples are precisely described by Raman spectroscopy. Figure 3 displays the S1 and S2 samples' recorded room-temperature Raman spectra in the 4000–50 cm^{-1} region. Since there is no polarizability change, Ni face-centered cubic (FCC) metal essentially exhibits a single-atom primitive unit cell and does not show any bands in the Raman spectra of the S1 and S2 samples. This observation could be attributed to the interaction between the electric field of the monochromatic light and the dipole moment within the material [25,26]. On the other hand, the Raman spectra of the synthesized composites show five bands related to the cubic NiO structure. These bands were observed at 209, 370, 544, 696, and 1070 cm^{-1}. The Raman bands of NiO below 600 cm^{-1} are generally owing to first-order phonon scattering, and the bands above 600 cm^{-1} are due to second-order scattering [27]. The Raman band at 370 cm^{-1} corresponds to one-phonon (1P) transverse optical (TO) and surface optical (SO), while the band at 544 cm^{-1} corresponds to (1P) longitudinal optical (LO) of NiO vibrational modes [28,29]. Moreover, The Raman bands at 696 and 1070 cm^{-1} correspond to two-phonon (2P) 2TO and 2LO of NiO vibrational modes, respectively [4,5]. The bands at 103 and 209 cm^{-1} that were found in the Raman spectra of the S1 and S2 samples could be attributed to the zone-boundary phonon mode [30]. The existence of LO and SO modes can be attributed to the disorder induced by surface imperfectness and the parity breaking defects in NiO, which arise due to nickel vacancy concentration [28,29]. The S1 sample's recorded Raman bands have a higher intensity compared to the S2 sample's, confirming that the S1 sample holds more NiO than the S2 sample contains. This finding is consistent with FTIR and XRD results. Although the presence of carbon has been confirmed through FTIR and will be confirmed through EDS as well, Raman spectra do not contain bands, indicating the possibility of the presence of highly amorphous carbon.
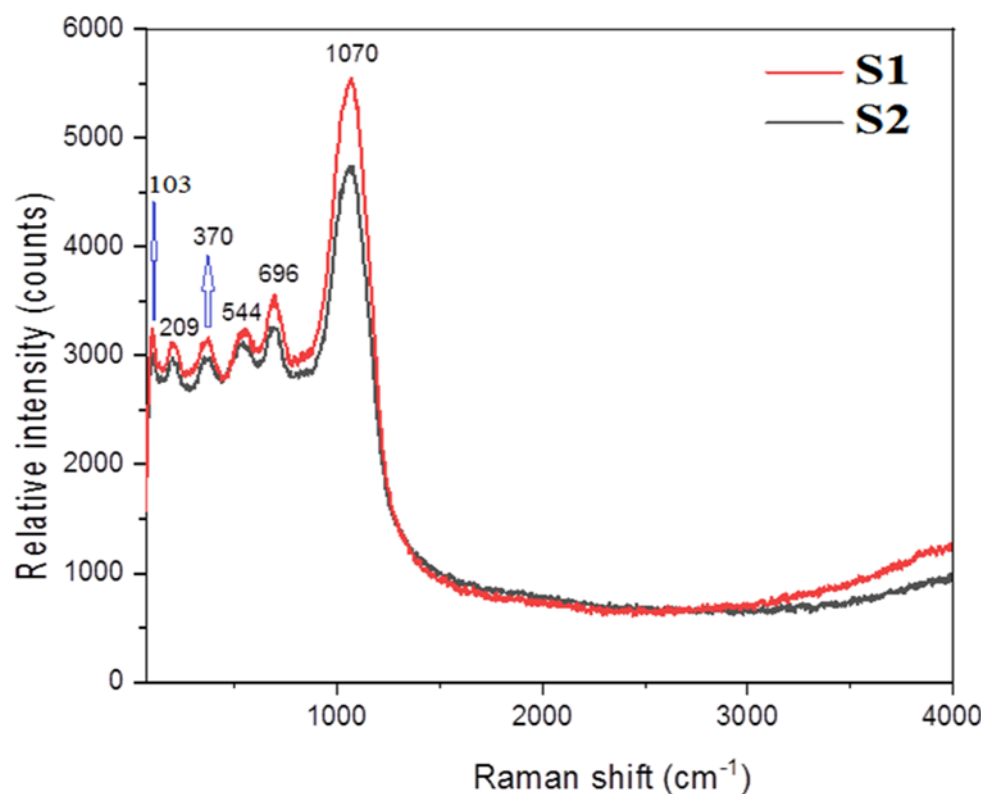
Figure 3. Raman spectra of the S1 and S2 samples.

3.4. Morphology and Elemental Analyses

The morphological and elemental examination of the investigated composites, illustrated in Figure 4, was evaluated using SEM and EDS techniques. Figure 4a,b provides an easy-to-understand representation of a structure that appeared to represent a network with voids of irregular shapes. This network's structure appears to be composed of particle clusters that are separated by holes of different sizes. From the above-mentioned description, it can be said that the preparation method used led to polyhedron structures consisting of various particles. The particles are strongly agglomerated, leading to a range of levels. These particles have differently shaped and nano-sized semi-spherical, oval, and cuboidal particles.

Figure 4c,d shows the composite's EDS pattern. This figure illustrates the presence of the signal-defining elements of nickel (Ni), carbon (C), and oxygen (O) in the prepared composites. The percentages of C, O, and Ni elements were found to be (6.12 and 13.88), (13.78 and 35.06), and (80.09 and 51.05) wt%, respectively, indicating the formation of Ni–NiO@C composites inside the S1 and S2, respectively.

Further details on the morphological characteristics of the S1 and S2 samples were discovered using TEM examinations, as shown in Figure 5. The images in this figure include TEM and high-resolution TEM (RTEM) images, Fast Fourier transform (FFT) and inverse Fast Fourier transform (IFFT) data, selected area electron diffraction (SAED) results, and histograms of the crystallite size statistical distribution (HCSD) of the resulting samples. Figure 5a,b shows the TEM and HRTEM images of S1 and S2 samples, respectively. TEM images revealed that Ni cores (dark segments) were clearly encrusted in the layers of the NiO structure (gray segments), which were coated by a carbon layer (white segments). These images support the core–double shell structures of Ni-NiO@C.
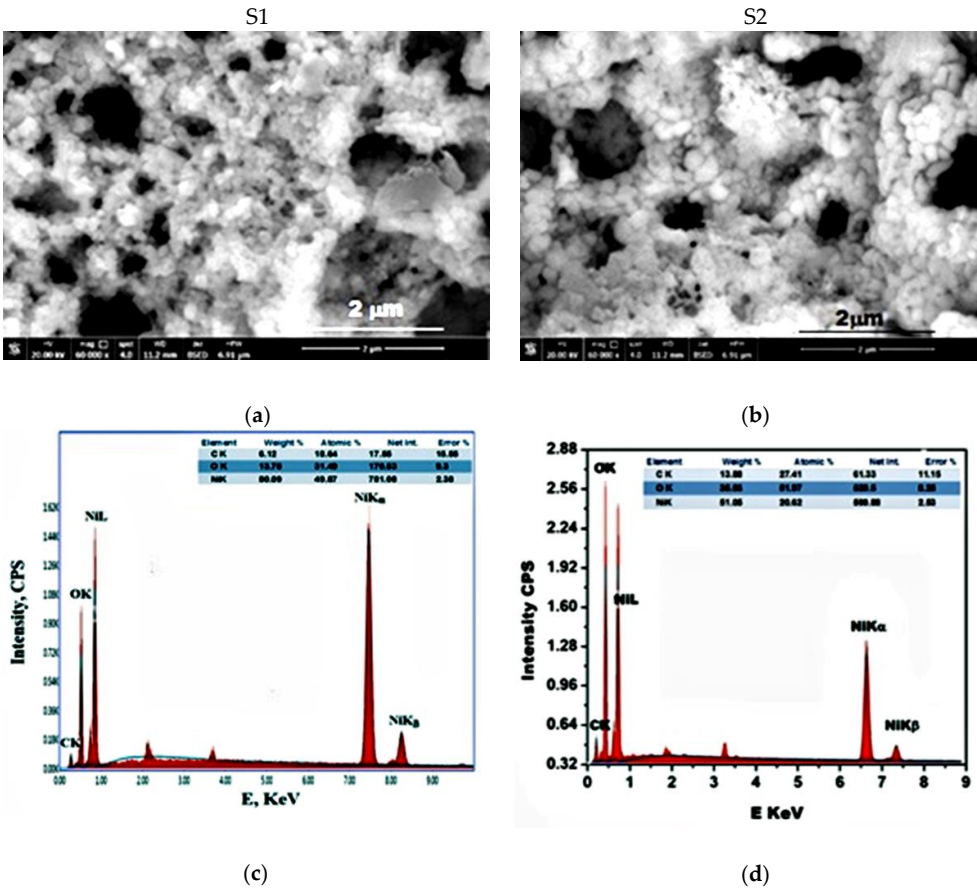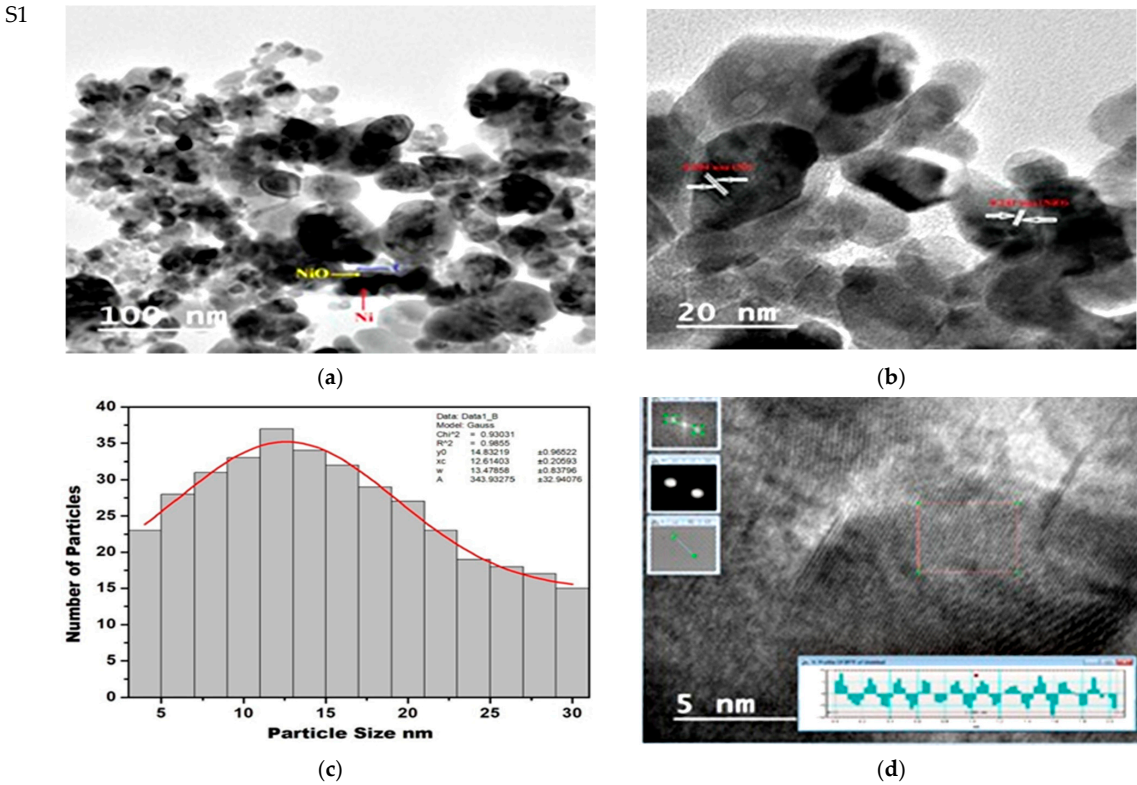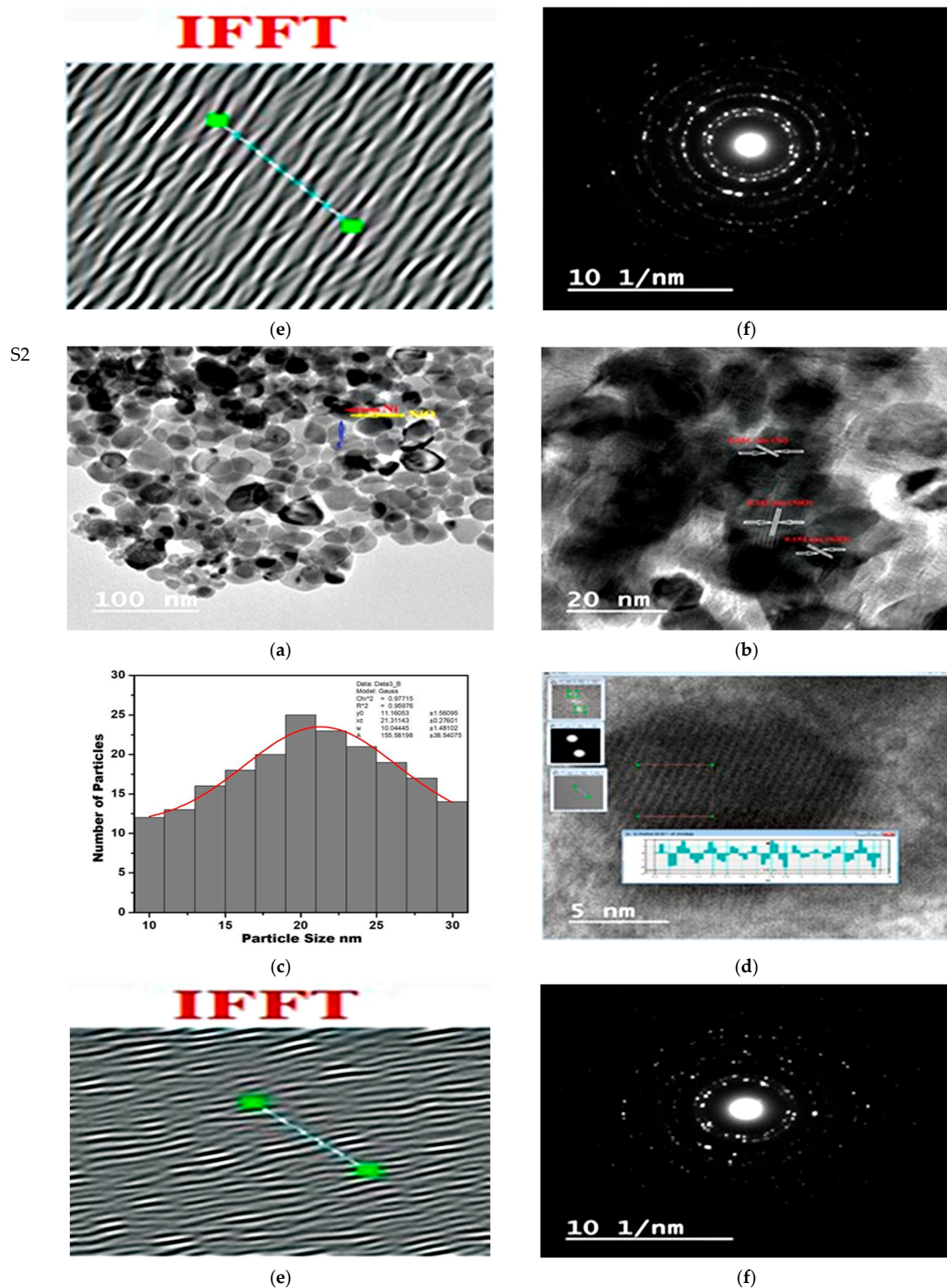
(a)

(b)

(c)

(d)

Figure 4. SEM (**a**,**b**) and EDS (**c**,**d**) of the S1 and S2 samples.

(a)

(b)

(c)

(d)

Figure 5. *Cont.*

(e)

(f)

S2

(a)

(b)

(c)

(d)

(e)

(f)

Figure 5. TEM and HRTEM images: (**a**,**b**), particle size distributions: (**c**), FFT and IFFT images: (**d**,**e**) and SAED images: (**f**) for samples S1 and S2.

The HRTEM images of S1 and S2 samples display a few clear lattice fringes with plenty of disorder. The HRTEM images of these samples showed that their nanoparticles (Ni and NiO) were highly crystalline. According to earlier XRD studies, this shows a significant level of lattice flaws. By contrast, it was discovered that the Ni core and NiO shell were connected at the local level through an atom-level interface. However, the interplanar

spacing of 0.204 and 0.241 nm, which particularly correspond to the (111) plane of Ni and the (111) plane of NiO, respectively, confirms the continuous transition or coherent bonding of the two phases (Ni and NiO). It is possible to attribute the interaction between NiO or Ni and the carbonaceous material to the presence of epoxide and hydroxide groups on the carbon surface, which produce active reaction sites [1]. The construction of HCSD based on TEM pictures, which provide deeper tools than SEM images, was required to provide insight into the particle size of the composite grains. The average particle size of the S1 and S2 composites is shown in Figure 5c to be 13 and 21 nm, respectively. FFT and IFFT were utilized to process the high-resolution images of the S1 and S2 samples in order to see the defective lattice in the composites as they were created. Figure 5d,e displays the IFFT and FFT patterns for the S1 and S2 samples, respectively. The coexistence of Ni and NiO crystallites is confirmed by FFT patterns, which demonstrate that the interplanar spacing of 0.204 and 0.154 nm corresponds to the (111) plane of Ni and the (220) plane of NiO, respectively. This is consistent with what is shown in Figure 5b for the S1 and S2 samples with regard to the interplanar spacing mentioned previously. IFFT patterns show uncompleted planes and areas of dislocation. A detailed microstructure analysis using IFFT confirms the presence of defects and dislocations in the as-prepared samples. These findings are consistent with the XRD results in Table 1. The dislocations and microstrains could be attributed to the investigated preparation method and the coexistence of Ni and NiO phases.

Figure 5f shows the SAED pattern of the S1 and S2 samples, respectively. This pattern confirms that Ni–NiO/C particles are polycrystalline. The continuous rings in these patterns with large light spots indicate the heterogeneous size of these nanoparticles. These findings strongly confirm the success of preparing Ni–NiO/C nanocomposites using a safe and environmentally friendly combustion method.
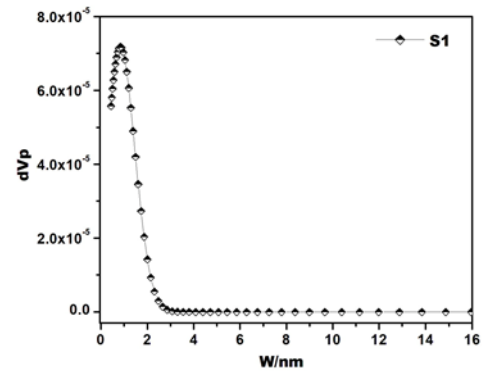
3.5. Surface Properties

As shown in Figure 6a, the N_2-adsorption/desorption isotherms at 77 K was employed for estimating the surface characteristics of the composites under investigation. By examining the isotherm drawn in this figure, it was found that they belong to type II with a type H3 hysteresis loop according to universally recognized authorities on chemical nomenclature and terminology (IUPAC) classifications. In particular, the surface properties—namely S_{BET}, V_p, and $\hat{r}$, and the C-constant values of the S1 and S2 samples are listed in Table 2. It is interesting to note that this isotherm's characteristics show that the composite as formed is micro- and mesoporous as a result of capillary condensation beginning at $P/P_o = 0.45$. The shape of the isotherm with a jump in the adsorption process at high relative pressure ($P/P_o = 0.85$–0.93) is shown in Figure 6a, which confirms the condensation process in interparticle voids. These voids were observed in the SEM images of the composites studied. However, the presence of micropores led to a jump in the adsorption process at low relative pressure ($P/P_o = 0.025$). The investigated composites have a larger hysteresis loop area, showing multilayer desorption from solid pore walls. Furthermore, the H3 hysteresis loop's form reveals slit-like pores or plate-like particles. Due to a reduction in their total pore capacity, as indicated in Table 2, the composites produced generally had a low surface area. However, increasing the amount of olive leaves caused the overall pore volume to rise, which in turn caused the surface area to rise, as was seen in the S2 sample. In order to describe the pore size distribution for the composite as it has been made, non-local density functional theory (NLDFT) needed to be used to adsorb nitrogen into pores. Histograms of the porosity or pore size distribution for these samples are shown in Figure 6b. According to the pores observed with one model distribution, the majority of the pores in the composite are microporous and range in size from 0.6 to 0.8 nm.
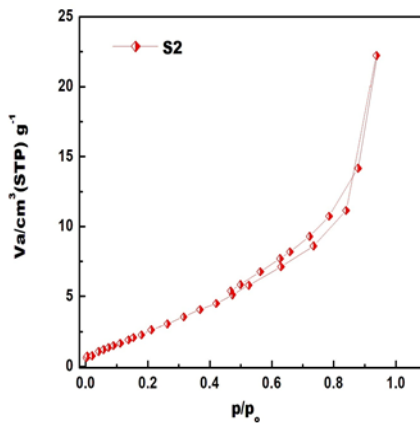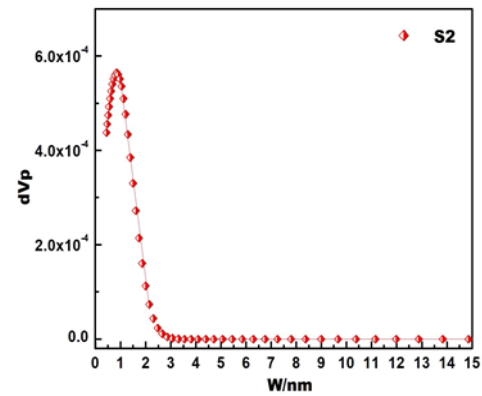
S1
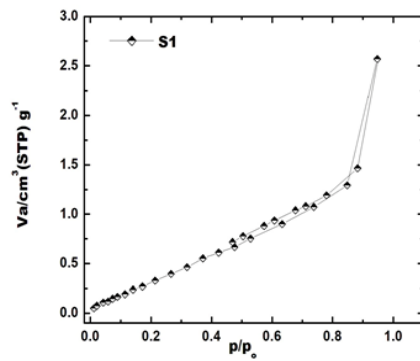
(a)

(b)

S2

(c)

(d)

Figure 6. (**a–d**) are the nitrogen adsorption isotherms and porous dimension distribution for the S1 and S2 specimens.

Table 2. Surface properties of the S1 and S2 samples.

Parameters	S_{BET} (m^2/g)	V_m (cc/g)	V_p (cc/g)	$\hat{r}$ (nm)	C-Constant
S1	4.3572	7.66	0.00397	0.4764	2.073
S2	14.259	3.276	0.0344	9.638	6.141

3.6. Magnetic Properties

The magnetization of the as-prepared composites (S1 and S2) can be observed in Figure 7, as it was determined at room temperature in a ±20 KOe magnetic field. By having an S-shaped magnetization curve at a local temperature, the investigated composites demonstrate ferromagnetic behavior. The magnetic parameters—namely, M_s, M_r, M_r/M_s, and H_c—of the as-prepared composites are presented in Table 3. However, the values of magnetization and coercivity enabled us to calculate the anisotropy constant ($K_a = H_c M_s/0.98$) for this composite [31]. The composite had small values for M_s, M_r, M_r/M_s, and Hc. Comparable results were observed while the Ni/NiO composite was developed, using Corchorus olitorius leaves [1]. However, the magnetic parameter values of the S2 sample (M_s, M_r, M_r/M_s, H_c, and K_a) were higher than those of the S1 sample.
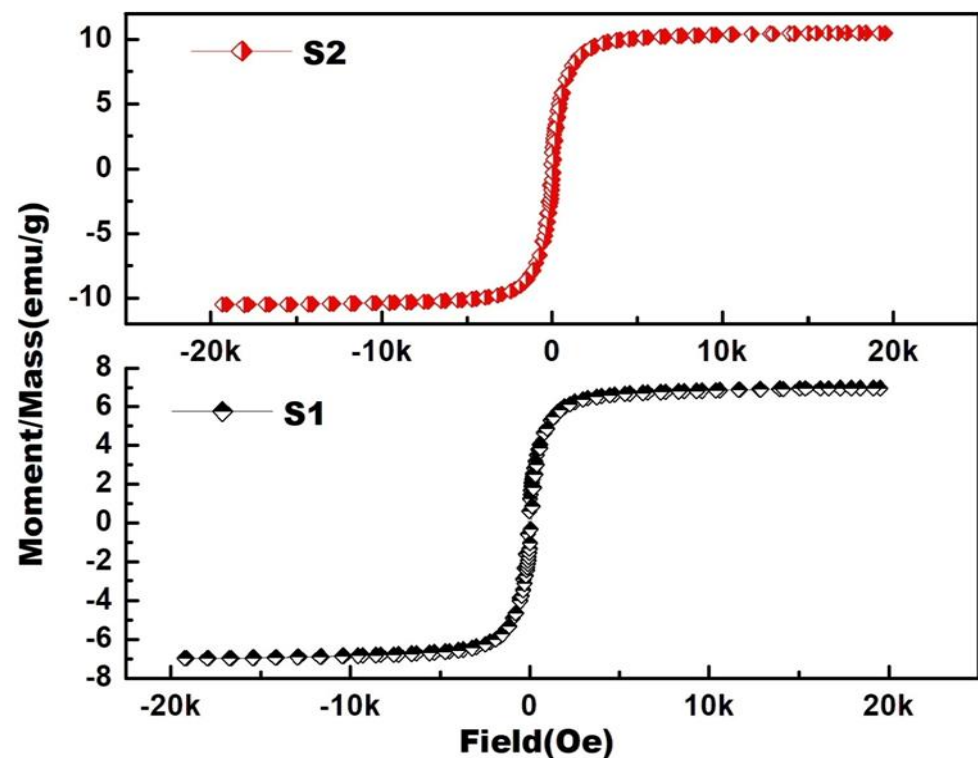
Figure 7. Magnetic hysteresis loops of the S1 and S2 samples.

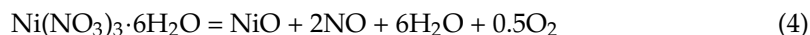**Table 3.** Magnetic properties of the S1 and S2 samples.

Parameters	M_s (emu/g)	M_r (emu/g)	M_r/M_s	H_c (Oe)	K_a (erg/cm^3)
S1	4.8744	1.229	0.2521	55.203	6.1129
S2	8.648	1.290	0.1492	39.639	349.79

4. Discussion

Nickel-based materials have gained great importance due to their catalytic, magnetic, and biological properties. Nickel nanoparticles can be produced by various methods such as these: Sol-gel, microemulsion, polyol, hydrazine-based reduction, laser ablation, and ultrasound-based reduction [31–35]. Despite the reality that the fabrication of magnetic metallic nickel nanostructure materials is economical and solely requires basic equipment, these procedures are challenging because of their oxidation and instability. This prompted the researchers to focus their efforts on finding ways to produce metallic nickel that would simultaneously prevent oxidation and retain stability. Indeed, pure metallic nickel nanoparticles and Ni/NiO nanocomposites have been obtained using the glycine-mediated combustion method [18]. In addition, a Ni/NiO nanocomposite has also been prepared using the dried leaves of a Corchorus olitorius-assisted combustion route [1]. It demonstrates that the dry plant part-based combustion approach has been recognized as a potential technique for creating metallic nanoparticles [1]. The procedures for the formation of metallic nickel material using the dry olive leaf-assisted combustion method can be discussed as follows:

(i)   The dry olive leaf powder acts as a biomaterial. Due to the presence of hydroxyl groups (OH) found in the phenols present in dry leaves, it holds and traps the bulk of nickel ions produced by the breakdown of nickel nitrate (Equation (4)) with the development of an organic–inorganic complex.

(ii)   The reduction of metallic salt (nickel nitrate) can be achieved by bioreduction-based biomolecules such as alkaloids, flavonoids, saponins, steroids, tannins, and other nutritional compounds [36].

(iii) The reduction, stabilization, and prevention of the oxidation of Ni nanoparticles are realized through carbon (Equation (5)), which is a protective agent of Ni, with the liberation of carbon dioxide (Equation (6)).

$$Ni(NO_3)_3 \cdot 6H_2O = NiO + 2NO + 6H_2O + 0.5O_2 \qquad (4)$$

$$NiO + C = Ni + CO \qquad (5)$$

$$CO + 0.5O_2 = CO_2 \qquad (6)$$

In other words, a fast decomposition of the precursors in the presence of biofuel (dry olive leaf powder) brought about the formation of a Ni/NiO nanocomposite with subsequent carbon formation. The olive leaf-mediated combustion route enhances a more reductive atmosphere, leading to an increase in Ni content [1]. Indeed, XRD analysis confirms the formation of crystalline Ni and NiO phases. EDS measurement indicates that the composites contain 6.12–13.88 wt% carbon elements. However, in FTIR analysis, four bands located at 418, 556, 660, and 1023–991 cm^{-1} are due to the metal–oxygen vibration mode. In addition, Raman spectra of the as-prepared composites confirm the presence of the NiO phase. Similar investigations were observed with different systems, indicating the role of carbon [36–38]. In such investigations, it was presupposed that the reduction of the ions that resulted from the breakdown of the precursor would lead to the creation of metallic nickel, which would subsequently be shielded by graphite.

SEM images both demonstrate that the average particle size of the Ni–NiO@C composite is larger than 100 nm, despite the fact that both Ni and NiO crystallite sizes are remarkably small and less than 100 nm as shown in TEM photos. This discrepancy could be explained by the creation of components with complicated geometries and distinctive, highly adaptable microstructures. This can be discussed with the "shrinking core" as a common model for the mechanism of the production of the Ni phase during the reduction pathway [39–41]. According to this model, the chemical reaction zone moves frontally, deep into the initial phase (NiO) [42–45]. Beginning with a full transformation of the outer layer of the NiO particle into lesser oxides or the metal itself (Ni) as reaction products, reduction takes place on the surface of the NiO particle. As a result, the inner core of the original substance is encircled by one or more reaction product shells, forming a core–shell with an increase in the size of the resulting particles. Therefore, the composite particles appeared in a polyhedral form that included spherical, oval, and cubic particles of different sizes, some of which exceeded the nanoscale. Depending on what is stated in the literature, the difference in the size of the product and its departure from the nanoscale may be due to the parallel surface defect dipole containing strong repulsive interactions, however the valence reduction and unpaired electron orbital at the outer surface may be [46–50]. These interpretations are consistent with our results, as it was found that the strain and dislocation of Ni are greater than those in NiO, which has a unit cell volume greater than that of metallic nickel. However, it was found in Table 2 that the surface area of the formed composite (S1) is small as a result of its relatively large grain size, which led to a noticeable decrease in its total pore volume in the presence of ultra-microspores.

In fact, pure NiO nanoparticles often show antiferromagnetic (AFM) behavior, while Ni nanoparticles display a ferromagnetic (FM) character [6]. Nevertheless, non-stoichiometric NiO nanoparticles have paramagnetic behavior at room temperature due to surface disorder, which arises from the presence of Ni^{3+} ions in the NiO lattice [1]. However, the weak ferromagnetic (FM) or superparamagnetic (SPM) behavior of NiO could be attributed to an exchange interaction between two neighboring Ni^{2+} ions through an oxygen ion, leading to a superexchange interaction. In the Ni/NiO system, the combination of ferromagnetic (FM) and antiferromagnetic (FM and AFM) constituents resulted in a tuning of both M_S and H_C [51]. In this study, the investigated composite had a M_s of 8.648 emu/g for the S2 sample—slightly higher than the same composite prepared by using *Corchorus olitorius*

leaves (6.977 emu/g), which was similar to the magnetism of the S1 sample [1]. In addition, the coexistence of ferro- and antiferromagnets (FM and AFM) due to the interface between two magnetically different (Ni and NiO) phases resulted in the appearance of the exchange bias (EB) effect [40]. It is clear that the squareness (M_r/M_s) is less than the value of 0.5, indicating that the particles interact via magnetostatic interaction and the anisotropy in the crystal lattice [52,53]. The composites (S1 and S2) investigated had moderate coercivity (55.203 and 39.639 Oe, respectively) due to the presence of magnetocrystalline anisotropy, shape anisotropy, and AFM-FM exchange coupling. In addition, the decreasing trend of the anisotropic constant (K_a) value in the S1 sample indicated a decrease in the magnetostatic energy of the composites and vice versa as shown in S2 sample [54]. These results indicate the complexity of the ensuing magnetic characteristics of the Ni–NiO/C composites due to the interaction of size, surface, and interface effects. Finally, Ni–NiO/C composites with a room-temperature FM character (RTFM) can be utilized as soft electromagnetic materials in the construction of transformers, cathode materials in batteries, and heterogeneous catalysis [6].

5. Conclusions

Ni–NiO/C nanocomposites were successfully prepared by using the dry olive leaf combustion method. The prepared composites were characterized using XRD, FTIR, Raman, SEM-EDS, and TEM analyses. Surface and magnetic properties were investigated for Ni–NiO/C composites. It was discovered that the constructed systems only contained crystalline Ni and NiO phases and that there were absorption bands connected to carbon groups as shown in FTIR analysis. The composites contained Ni, C, and O elements, according to EDS analysis, and TEM and SEM examinations showed that the formation particles exhibited a wide variety of sizes and shapes. Additionally, these findings revealed that the investigated composites had a low surface area due to a decrease in the total pore volume. It exhibited low magnetism and coercivity. Additionally, the composite's squareness was below 0.5, indicating that the interactions between the constituent parts were caused by anisotropy in the crystal lattice and magnetostatic interaction.

These results are very encouraging, so further experiments in various applied sectors are recommended.

Author Contributions: Conceptualization, O.H.A.-E., M.N. (Mohamed Nasrallah) and G.M.A.-S.; methodology, F.F.A.-F.; software, O.H.A.-E.; validation, O.H.A.-E., M.N. (Mai Nasrallah) and G.M.A.-S.; formal analysis, O.H.A.-E.; investigation, M.N. (Mohamed Nasrallah) and M.N. (Mai Nasrallah); resources, O.H.A.-E.; data curation, G.M.A.-S.; writing—original draft preparation, O.H.A.-E., G.M.A.-S., M.N. (Mai Nasrallah) and M.A.; writing—review and editing, O.H.A.-E., M.N. (Mohamed Nasrallah), M.N. (Mai Nasrallah) and M.A.; visualization, O.H.A.-E., G.M.A.-S. and M.A.; supervision, O.H.A.-E.; project administration, O.H.A.-E. and G.M.A.-S.; funding acquisition, G.M.A.-S., M.A. and F.F.A.-F. All authors have read and agreed to the published version of the manuscript.

Institutional Review Board Statement: Not applicable.

Informed Consent Statement: Not applicable.

Data Availability Statement: The data presented in this study are available on request from the corresponding author.

Conflicts of Interest: The authors declare no conflict of interest.

References

1. Deraz, N.M. Incandescent combustion synthesis of nanomagnetic Ni/NiO composites. *Sci. Sinter.* **2021**, *53*, 155–167. [CrossRef]
2. Al-Senani, G.M.; Abd-Elkader, O.H.; Al-Kadhi, N.S.; Deraz, N.M. Effect of the Glycine Treatment on Synthesis and Physicochemical Characteristics of Nanosized Ni-Mn Mixed Oxides. *Crystals* **2021**, *11*, 487. [CrossRef]
3. Al-Senani, G.M.; Deraz, N.M.; Abd-Elkader, O.H. Magnetic and characterization studies of CoO/Co$_3$O$_4$ nanocomposite. *Processes* **2021**, *8*, 844. [CrossRef]
4. Deraz, N.M.; Abd-Elkader, O.H. Synthesis and Characterization of FeO/Ni$_{0.5}$Mn$_{0.5}$Fe$_2$O$_4$ Nano-Composite. *Asian J. Chem.* **2014**, *26*, 2141. [CrossRef]
5. Suzuki, M.; Kudo, K.; Kojima, K.; Yasue, T.; Akutsu, N.; Diño, W.A.; Kasai, H.; Bauer, E.; Koshikawa, T. Magnetic domain patterns on strong perpendicular magnetization of Co/Ni multilayers as spintronics materials: I. Dynamic observations. *J. Phys. Condens. Matter* **2013**, *25*, 406001. [CrossRef]
6. Motlagh, M.K.; Youzbashi, A.A.; Hashemzadeh, F.; Sabaghzadeh, L. Structural properties of nickel hydroxide/oxyhydroxide and oxide nanoparticles obtained by microwave-assisted oxidation technique. *Powder Technol.* **2013**, *237*, 562–568. [CrossRef]
7. Yao, X.-J.; He, X.-M.; Song, X.-Y.; Ding, Q.; Li, Z.-W.; Zhong, W.; Au, C.-T.; Du, Y.-W. Enhanced exchange bias and coercivity arising from heterojunctions in Ni–NiO nanocomposites. *Phys. Chem. Chem. Phys.* **2014**, *16*, 6925–6930. [CrossRef]
8. Nogués, J.; Langlais, V.; Sort, J.; Doppiu, S.; Suriñach, S.; Baró, M.D. Magnetic properties of Ni-NiO (ferromagnetic-antiferromagnetic) nanocomposites obtained from a partial mechanochemical reduction of NiO. *J. Nanosci. Nanotechnol.* **2008**, *8*, 2923–2928. [CrossRef]
9. Yan, X.; Tian, L.; Chen, X. Crystalline/amorphous Ni/NiO core/shell nanosheets as highly active electrocatalysts for hydrogen evolution reaction. *J. Power Sources* **2015**, *300*, 336–343. [CrossRef]
10. Song, S.; Yao, S.; Cao, J.; Di, L.; Wu, G.; Guan, N.; Li, L. Heterostructured Ni/NiO composite as a robust catalyst for the hydrogenation of levulinic acid to γ-valerolactone. *Appl. Catal. B* **2017**, *217*, 115–124. [CrossRef]
11. Sun, X.; Si, W.; Liu, X.; Deng, J.; Xi, L.; Liu, L.; Yan, C.; Schmidt, O.G. Multifunctional Ni/NiO hybrid nanomembranes as anode materials for high-rate Li-ion batteries. *Nano Energy* **2014**, *9*, 68–175. [CrossRef]
12. Liu, T.; Pang, Y.; Xie, X.; Qi, W.; Wu, Y.; Kobayashi, S.; Zheng, J.; Li, X. Synthesis of microporous Ni/NiO nanoparticles with enhanced microwave absorption properties. *J. Alloy. Compd.* **2016**, *667*, 287–296. [CrossRef]
13. Xiang, W.; Liu, Y.; Yao, J.; Sun, R. Influence of annealing temperature on the microstructure and magnetic properties of Ni/NiO core-shell nanowires. *Phys. E Low-Dimens. Syst. Nanostruct.* **2018**, *97*, 363–367. [CrossRef]
14. Chaghouri, H.A.; Tuna, F.; Santhosh, P.N.; Thomas, P.J. Tiny Ni–NiO nanocrystals with exchange bias induced room temperature ferromagnetism. *Solid State Commun.* **2016**, *230*, 11–15. [CrossRef]
15. Sharma, K.R.; Sharma, H.; Negi, N.S. Synthesis and Characterizations of Pure Ni and Ni-NiO Composite Ceramic Annealed at Varied Temperatures. In *AIP Conference Proceedings, Bahal, India, 7–9 February 2019*; AIP Publishing: Melville, NY, USA, 2019; Volume 2142, p. 1.
16. Cabanas-Polo, S.; Bermejo, R.; Ferrari, B.; Sanchez-Herencia, A.J. Ni–NiO composites obtained by controlled oxidation of green compacts. *Corros. Sci.* **2012**, *55*, 172–179. [CrossRef]
17. Ekeroth, S.; Ikeda, S.; Boyd, R.D.; Shimizu, T.; Helmersson, U. Growth of semi-coherent Ni and NiO dual-phase nanoparticles using hollow cathode sputtering. *J. Nanoparticle Res.* **2019**, *21*, 37. [CrossRef]
18. Deraz, N.M. Magnetic behavior and physicochemical properties of Ni/NiO nanoparticles. *Curr. Appl. Phys.* **2012**, *12*, 928–934. [CrossRef]
19. Madhumitha, G.; Reopen, S.M. Devastated crops: Multifunctional efficacy for the production of nanoparticles. *J. Nanomater.* **2013**, *2013*, 951858. [CrossRef]
20. Kuppusamy, P.; Yusoff, M.M.; Maniam, G.P.; Govinda, N. Biosynthesis of metallic nanoparticles using plant derivatives and their new avenues in pharmacological applications—An updated report. *Saudi Pharm. J.* **2016**, *24*, 473–484. [CrossRef]
21. Cullity, B.D. *Elements of X-ray Diffraction*; Addison-Wesley Publishing Co., Inc.: Boston, MA, USA, 1956.
22. Kavaliauskas, Ž.; Marcinauskas, L.; Valatkevicius, P. Formation and Characterization of Carbon and Nickel Oxide/Carbon Composites for Supercapacitors. *Acta Phys. Pol. A* **2011**, *119*, 253–255. [CrossRef]
23. Ghaemi, F.; Abdullah, L.C.; Tahir, P. Core/shell structure of Ni/NiO encapsulated in carbon nanosphere coated with few-and multi-layered graphene: Synthesis, mechanism and application. *Polymers* **2016**, *8*, 381. [CrossRef] [PubMed]
24. Abd-Elkader, O.H.; Deraz, N.M.; Aleya, L. Rapid Bio-Assisted Synthesis and Magnetic Behavior of Zinc Oxide/Carbon Nanoparticles. *Crystals* **2023**, *13*, 1081. [CrossRef]
25. Lewis, I.R.; Edwards, H. *Handbook of Raman Spectroscopy: From the Research Laboratory to the Process Line*; CRC Press: Boca Raton, FL, USA, 2001.
26. Kwan, J.T.H.; Bonakdarpour, A.; Afonso, G.; Wilkinson, D.P. Bridging fundamental electrochemistry with applied fuel cell testing: A novel and economical rotating disk electrode tip for electrochemical assessment of catalyst-coated membranes. *Electrochim. Acta* **2017**, *258*, 208–219. [CrossRef]
27. George, G.; Anandhan, S. Synthesis and characterisation of nickel oxide nanofibre webs with alcohol sensing characteristics. *Rsc Adv.* **2014**, *4*, 62009–62020. [CrossRef]
28. Mironova-Ulmane, N.; Kuzmin, A.; Steins, I.; Grabis, J.; Sildos, I.; Pärs, M. Raman scattering in nanosized nickel oxide NiO. *J. Phys. Conf. Ser.* **2007**, *93*, 012039. [CrossRef]

29. Feng, C.; Kou, X.; Chen, B.; Qian, G.; Sun, Y.; Lu, G. One-pot synthesis of In doped NiO nanofibers and their gas sensing properties. *Sens. Actuators B Chem.* **2017**, *253*, 584–591. [CrossRef]

30. Mironova-Ulmane, N.; Kuzmin, A.; Sildos, I.; Puust, L.; Grabis, J. Magnon and phonon excitations in nanosized NiO. Latv. *J. Phys. Tech. Sci.* **2019**, *56*, 61–72.

31. Wu, X.; Xing, W.; Zhang, L.; Zhuo, S.; Zhou, J.; Wang, G.; Qiao, S. Nickel nanoparticles prepared by hydrazine hydrate reduction and their application in supercapacitor. *Powder Technol.* **2012**, *224*, 162–167. [CrossRef]

32. Dzidziguri, E.L.; Sidorova, E.N.; Yahiyaeva, J.E.; Ozherelkov, D.Y.; Gromov, A.A.; Nalivaiko, A.Y. Low-temperature oxidation of metal nanoparticles obtained by chemical dispersion. *Micro Nano Lett.* **2020**, *15*, 461–464. [CrossRef]

33. Chen, D.H.; Wu, S.H. Synthesis of Nickel Nanoparticles in Water-in-Oil Microemulsions. *Chem. Mater.* **2000**, *12*, 1354–1360. [CrossRef]

34. Pajor-Swierzy, A.; Socha, R.; Pawłowski, R.; Warszynski, P.; Szczepanowicz, K. Application of metallic inks based on nickel-silver core-shell nanoparticles for fabrication of conductive films. *Nanotechnology* **2019**, *30*, 225301. [CrossRef] [PubMed]

35. Sportelli, M.C.; Clemente, M.; Izzi, M.; Volpe, A.; Ancona, A.; Picca, R.A.; Palazzo, G.; Cio, N. Exceptionally stable silver nanoparticles synthesized by laser ablation in alcoholic organic solvent. *Colloids Surf. A* **2018**, *559*, 148–158. [CrossRef]

36. Adelere, I.A.; Lateef, A.A. Novel approach to the green synthesis of metallic nanoparticles: The use of agro-wastes, enzymes and pigments. *Nanotechnol. Rev.* **2016**, *5*, 567–587. [CrossRef]

37. Jeon, Y.T.; Moon, J.Y.; Lee, G.H.; Park, J.; Chang, Y. Comparison of the magnetic properties of metastable hexagonal close-packed Ni nanoparticles with those of the stable face centered cubic Ni nanoparticles. *J. Phys. Chem. B* **2006**, *110*, 1187–1191. [CrossRef] [PubMed]

38. Rodríguez-González, V.; Marceau, E.; Beaunier, P.; Che, M.; Train, C. Stabilization of hexagonal close-packed metallic nickel for alumina-supported systems prepared from Ni (II) glycinate. *J. Solid State Chem.* **2007**, *180*, 22–30. [CrossRef]

39. Dong, X.; Ji, X.; Wu, H.; Zhao, L.; Li, J.; Yang, W.J. Shape control of silver nanoparticles by stepwise citrate reduction. *Phys. Chem. C* **2009**, *113*, 6573–6576. [CrossRef]

40. Wang, W.; Zhang, Q.; Liu, Z.; Libor, Z. Highly efficient size reduction of nanoparticles by the shock wave method. *Funct. Mater. Lett.* **2010**, *3*, 299–302. [CrossRef]

41. Ji, X.; Song, X.; Li, J.; Bai, Y.; Yang, W.; Peng, X. Size Control of Gold Nanocrystals in Citrate Reduction: The Third Role of Citrate. *J. Am. Chem. Soc.* **2007**, *129*, 13939–13948. [CrossRef]

42. Bhattacharyya, R.; Bhanja, K.; Mohan, S. Mathematical analysis of reduction of copper oxide pellets by hydrogen using the shrinking core model. *Fusion Eng. Des.* **2015**, *100*, 560–564. [CrossRef]

43. Kar, P. A comparison of the pseudo-steady-state and shrinking-core model for the reduction of titanium dioxide to titanium. *J. Solid State Electrochem.* **2008**, *12*, 1611–1617. [CrossRef]

44. Villen-Guzman, M.; Paz-Garcia, J.M.; Arhoun, B.; Cerrillo-Gonzalez, M.M.; Rodriguez-Maroto, J.M.; Vereda-Alonso, C.; Gomez-Lahoz, C. Chemical Reduction of Nitrate by Zero-Valent Iron: Shrinking-Core versus Surface Kinetics Models. *Int. J. Environ. Res. Public Health* **2020**, *17*, 1241. [CrossRef] [PubMed]

45. Vilardi, G. Mathematical modelling of simultaneous nitrate and dissolved oxygen reduction by Cu-nZVI using a bi-component shrinking core model. *Powder Technol.* **2019**, *343*, 613–618. [CrossRef]

46. Li, L.; Chen, L.; Qihe, R.; Li, G. Magnetic crossover of NiO nanocrystals at room temperature. *Appl. Phys. Lett.* **2006**, *89*, 134102. [CrossRef]

47. Tsunekawa, S.; Ishikawa, K.; Li, Z.Q.; Kawazoe, Y.; Kasuya, A. Origin of anomalous lattice expansion in oxide nanoparticles. *Phys. Rev. Lett.* **2000**, *85*, 3440. [CrossRef] [PubMed]

48. Ayyub, P.; Palkar, V.R.; Chattopadhyay, S.; Multani, M. Effect of crystal size reduction on lattice symmetry and cooperative properties. *Phys. Rev. B* **1995**, *51*, 6135. [CrossRef] [PubMed]

49. Pitike, K.C.; Marquez-Rossy, A.E.; Flores-Betancourt, A.; Chen, D.; Santosh, K.; Cooper, V.R.; Lara-Curzio, E. On the elastic anisotropy of the entropy-stabilized oxide (Mg, Co, Ni, Cu, Zn) O compound. *J. Appl. Phys.* **2020**, *128*, 015101. [CrossRef]

50. Cabo, M.; Pellicer, E.; Rossinyol, E.; Estrader, M.; López-Ortega, A.; Nogués, J.; Castell, O.; Suriñach, S.; Baró, M.D. Synthesis of compositionally graded nanocast $NiO/NiCo_2O_4/Co_3O_4$ mesoporous composites with tunable magnetic properties. *J. Mater. Chem.* **2010**, *20*, 7021–7028. [CrossRef]

51. Kakazey, M.; Vlasova, M.; Vorobiev, Y.; Leon, I.; Gonzalez, M.C.; Urbiola, E.A.C. Processes of microstructural evolution during high-energy mechanical treatment of ZnO and black NiO powder mixture. *Phys. B Condens. Matter* **2014**, *453*, 116–122. [CrossRef]

52. Bakeer, D.E.S.; Abou-Aly, A.I.; Mohammed, N.H.; Awad, R.; Hasebbo, M. Characterization and Magnetic properties of nanoferrite $ZnFe_{2-x}La_xO_4$ prepared by co-precipitation method. *J. Supercond. Nov. Magn.* **2017**, *30*, 893–902. [CrossRef]

53. Stoner, E.C.; Wohlfarth, E.P. A mechanism of magnetic hysteresis in heterogeneous alloys. *Philos. Trans. R. Soc. London. Ser. A Math. Phys. Sci.* **1984**, *240*, 599–642. [CrossRef]

54. Gandhi, A.C.; Huang, C.Y.; Yang, C.C.; Chan, T.S.; Cheng, C.L.; Ma, Y.R.; Wu, S.Y. Growth mechanism and magnon excitation in NiO nanowalls. *Nanoscale Res. Lett.* **2011**, *6*, 485. [CrossRef] [PubMed]